

# Three-dimensional Near-field Anatomy Reveals Geometric Resonance of Hyperbolic Phonon Polariton Micro-Structures

Haomin Wang<sup>1</sup>, Jiahan Li<sup>2</sup>, James H. Edgar,<sup>2</sup> and Xiaoji G. Xu<sup>1\*</sup>

<sup>1</sup>Department of Chemistry, Lehigh University, Bethlehem, PA 18015, USA

<sup>2</sup>Tim Taylor Department of Chemical Engineering, Kansas State University, Manhattan, KS 66506,

USA

Email: xgx214@lehigh.edu

## Abstract

Standing waves of defined momentum arise when the propagating wave is confined by finite boundaries of suitable dimensions and symmetry. Phonon polaritons, often supported by two-dimensional materials, are waves formed from hybridization of collective phonon oscillations and electromagnetic field. Polaritons propagate with short wavelengths and high field confinement and are the basis for nano-photonic devices. Here, we perform near-field anatomy of isotopically pure hexagonal boron nitride ( $h$ -<sup>11</sup>BN) micro-disk and a reflective edge from three-dimensional near-field response cubes obtained by the peak force scattering-type near-field optical microscopy (PF-SNOM). Momentum quantization of polaritonic standing wave is revealed *in situ* from the confinement of the circular microstructures. The distance between near-field tip and sample can fine-tune the momentum of polaritons, and modifying the superposition of polaritonic standing wave modes. The three-dimensional near-field anatomy can be expanded to other polariton-supporting materials, evaluating geometrical resonances *in situ* toward the betterment of nano-photonic devices.

## Introduction

Phonon polaritons (PhPs), quasi particles from a hybrid of electromagnetic (EM) wave and

collective phonon oscillations, have been a research focus of nanophotonics. Utilization of PhPs holds the promise for bridging electronic and photonic technologies in infrared frequencies.<sup>1</sup> PhPs propagate along the interface of the materials with opposite signs of the real part of the dielectric function,<sup>2</sup> or in the volume of hyperbolic materials.<sup>3</sup> PhPs have much more compressed wavelength than free-propagating photons, leading to a locally enhanced EM field. Recent advances of two-dimensional (2D) materials provide a range of new polariton-supporting materials.<sup>1</sup> Hexagonal boron nitride (*h*-BN) supports surface phonon polaritons and hyperbolic phonon polaritons and has been a fundamental material for the development of nanotechnology based on polaritons.<sup>4-6</sup>

The short wavelength of the polaritons is associated with high momentum, and cannot be directly coupled from free-space propagating photons due to the restriction from phase matching.<sup>7</sup> Scattering-type scanning near-field optical microscopy (s-SNOM) is a popular scanning probe microscopy technique that can both excite and detect PhPs. The metallic atomic force microscope (AFM) tip locally enhances EM field at its apex with high spatial frequencies and is capable of effectively exciting polaritons in 2D materials. The excitation of polaritons modifies the scattering properties of the AFM tip, leading to changes of amplitude and phase of the scattered light, but not frequency. To detect the near-field signal from the far-field background of same optical frequency, the AFM cantilever is externally driven to oscillate at its mechanical resonance in tapping mode AFM. The scattered light from the AFM tip is optically detected and demodulated by a lock-in amplifier at a non-fundamental harmonic of the cantilever oscillation frequency, from which extracts s-SNOM signal.

The operation mechanism of s-SNOM demarcates its limitation: the near-field generated

from s-SNOM is an average of near-field responses at different tip-sample distances of the tip oscillation. Different tip-sample distances correspond to different spatial confinement of EM field underneath the AFM tip, thus leading to different excitation conditions (Figs. 1a-b). However, s-SNOM only provides one-value signal associated with a demodulation order, thus only yielding a near-field image in two lateral dimensions, rather than providing three-dimensional (3D) near-field responses with both lateral and vertical Cartesian coordinates. More information about polaritons in photonic nanostructures can be obtained, if all three dimensions of near-field responses are available. Here, we utilize a new type of near-field microscopy, the peak force scattering-type near-field optical microscopy (PF-SNOM),<sup>8</sup> to obtain a 3D near-field response cube of polaritonic isotopically pure  $h$ -<sup>11</sup>BN microstructures. We perform near-field anatomy along the tomographic and sectional profiles of the 3D response cube at a series of infrared frequencies, revealing subtleties of phonon polaritons through correlations that were not previously available for s-SNOM.

### **Method to Collection of 3D near-field Response Cube**

PF-SNOM operates with the peak force tapping (PFT) mode of AFM. The vertical position of the sample is oscillating at a low frequency ( $\sim 4$  kHz) that is much below the resonant frequency of the AFM cantilever. Under PFT mode, instantaneous tip-sample distance is deterministic from the extension of the piezoelectric sample stage and the dynamic deflection of the AFM cantilever. PF-SNOM simultaneously measures the scattered light signal from tip-sample region and the instantaneous tip-sample distance (Fig. 1c). The relation of the tip-sample distance versus raw scattering signal from the tip is obtained through a correlation of signal waveforms in the time domain (Fig. 1d). Because the oscillation amplitude of the tip-

sample distance in PFT mode spans more than a hundred nanometers, a linear far-field background fit can be performed on the region of large tip-sample distances where the near-field signal is negligible. The resulting linear background is back extrapolated to all tip-sample distance and to be removed from the raw tip scattering signal. The result is a vertical near-field interaction curve with an explicit tip-sample distance dependence (Fig. 1e).

Vertical near-field interaction curves at every lateral scanned position are then assembled to form a 3D near-field response cube. The 3D near-field response cube  $S_{NF}(x, y, d)$  includes near-field signals  $S_{NF}$  at each lateral scanned position  $(x, y)$ , as well as each tip-sample distance  $d$  (Fig. 1f). We collect many 3D near-field response cubes at a series of infrared frequencies. In the near-field anatomy, the collected 3D near-field response cube is analyzed on the tomographic (with fixed  $d$ ) and sectional (with fixed  $x$  or  $y$ ) directions to reveal correlations between the spatial frequencies and the excitation frequency.

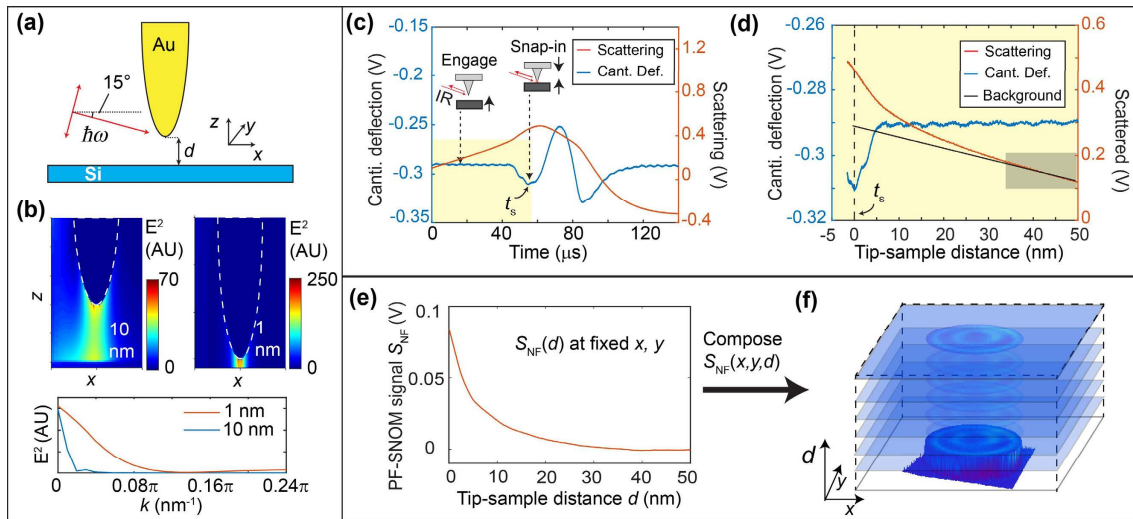


**Figure 1.** FDTD simulation on the effect of tip-sample distance and explicit tip-sample distance information in PF-SNOM. (a) The scheme used in FDTD simulation. (b) FDTD simulations of EM field enhancements with  $d = 10$  and  $1$  nm under  $1403$   $\text{cm}^{-1}$  illumination. FFTs of signal profile along  $x$ -axis in the angular momentum  $k$ -space are plotted in the lower panel. Shorter tip-sample distance couples with higher momenta. (c) Simultaneously obtained

cantilever deflection and scattered light from the tip-sample region during one cycle of peak force tapping. Insets schematically illustrates the tip-sample distance during PFT. The PF-SNOM sampling region is right before the snap-in time point  $t_s$ . (d) Cantilever deflection curve, scattered light and linearly fitted background shown in the tip-sample distance domain at the yellow region in (c).  $t_s$  corresponds to  $d = 0$  which is indicated by a vertical dashed line. The grey shadow indicates the background fitting range. Data in (c-d) are obtained on the Au surface at  $1600 \text{ cm}^{-1}$ . (e) A typical vertical near-field interaction curve. (f) A 3D near-field response cube is formed by assembling vertical interaction curves.

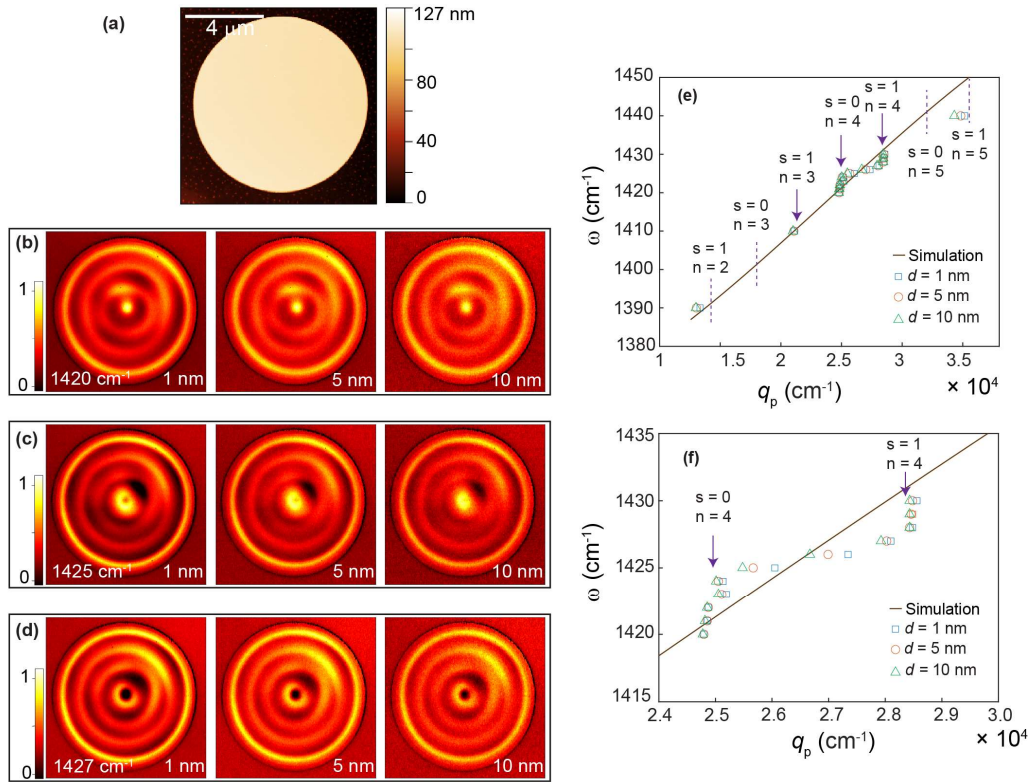


**Figure 2.** Fringe patterns and vertical near-field responses of the  $h$ - $^{11}\text{BN}$  micro-resonator through near-field anatomy. (a) AFM topography of an  $h$ - $^{11}\text{BN}$  micro-disk resonator with a diameter of  $9 \mu\text{m}$  and a thickness of  $70 \text{ nm}$ , the scale bar is  $4 \mu\text{m}$ . (b-d) Normalized tomographic PF-SNOM images at tip-sample distances  $d = 1, 5$  and  $10 \text{ nm}$  (in column) and at  $\omega = 1420, 1425$  and  $1427 \text{ cm}^{-1}$  (in row). In (c) and (d), positions of fringes shift inward as  $d$  increases. (e) The  $\omega - q_p$  dispersion relation of the  $h$ - $^{11}\text{BN}$  micro-disk extracted from PF-SNOM results. Experimental data (blue squares, red circles, and green triangles) are overlaid with calculated dispersion relation (brown curve). Calculated  $k_{sn}$  correspond to three observed resonant conditions are shown as purple arrows, others are shown as dashed purple lines. Mode numbers  $(s, n)$  are displayed along with resonant conditions. Details in the  $1420\text{-}1430 \text{ cm}^{-1}$

range are shown in (f).

## Results

### Tomographic Analysis Near-field Responses

We investigate a circular micro-disk and a reflective edge made of the isotopically pure hexagonal boron nitride ( $h\text{-}^{11}\text{BN}$ ).<sup>9</sup> Hexagonal boron nitride is a two-dimensional van der Waals material that supports hyperbolic phonon polaritons (HPhPs).<sup>10-19</sup> Isotopically pure  $h\text{-}^{11}\text{BN}$  is advantageous over regular  $h\text{-BN}$  in that it has smaller damping from the phonon relaxation, which leads to a longer polariton propagation length.<sup>20</sup> The investigated  $h\text{-}^{11}\text{BN}$  micro-disk is 9  $\mu\text{m}$  in diameter and 70 nm in thickness as revealed by the AFM topography image (Fig. 2a). 3D near-field response cubes are collected with PF-SNOM at a series of infrared frequencies. Tomographic  $x\text{-}y$  near-field images from response cubes at three tip-sample distances ( $d$ ) and three frequencies ( $\omega$ ) are displayed in Figs. 2b-d.

At first glance, circular fringes of the tomographic images from PF-SNOM resemble what one would obtain from regular s-SNOM with the high order lock-in demodulation (see Supplementary Fig. S1). However, tomographic images at different tip-sample distances  $d$  reveal additional details that are missing from regular s-SNOM images. As  $d$  is increased from 1 to 10 nm, the spatial patterns of the tomographic images evolve and is dependent on the infrared frequency  $\omega$ . For  $\omega = 1420\text{ cm}^{-1}$ , the fringe patterns do not exhibit noticeable changes. However, fringe patterns at  $\omega = 1425$  and  $1427\text{ cm}^{-1}$  exhibit discernable changes: as  $d$  increases, the central hole disappears or shrinks, indicating a change of spatial frequency of PhPs.

We then extract the periodicity of the circular fringes of the  $h\text{-}^{11}\text{BN}$  disk to obtain the

energy versus momentum dispersion relations (Fig. 2e and 2f). Details of the extracting method are described in the Supplementary Fig. S2. The experimental dispersion relation exhibits an interesting behavior: the polariton momentum exhibits a fixed value at  $2.5 \times 10^4$  and  $2.85 \times 10^4 \text{ cm}^{-1}$  regardless of the change of tip-sample distance  $d$  over a small range of infrared frequency; between these two fixed values, the momentum of polariton changes with  $d$ ; larger  $d$  corresponds to lower spatial frequencies of the polariton at a given excitation energy. The dispersion relation of the  $h$ - $^{11}\text{BN}$  disk clearly deviates from the theoretical prediction of  $h$ - $^{11}\text{BN}$  layer that lacks the geometrical confinement.<sup>21</sup> To confirm this is a general behavior of circular micro-disk of  $h$ - $^{11}\text{BN}$ , we performed PF-SNOM measurement on another circular disk of different thickness, a similar behavior was found (see Supplementary Fig. S3).

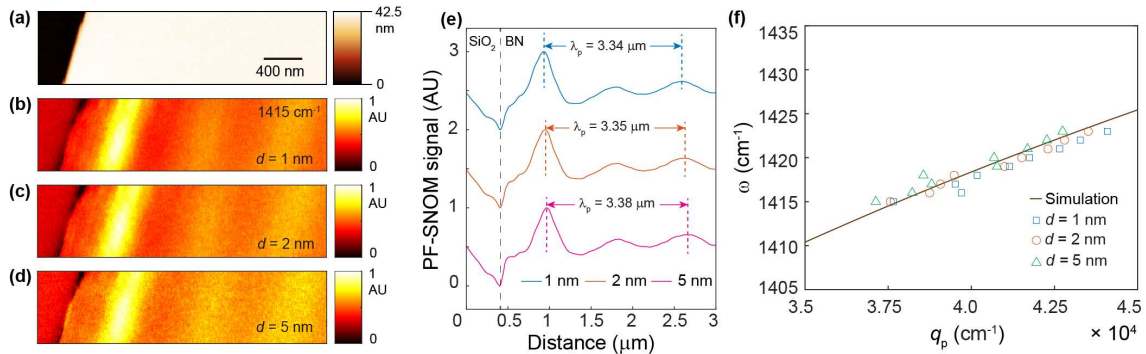


**Figure 3.** Near-field anatomy on the edge of an  $h$ - $^{11}\text{BN}$  flake. (a) The topography of an  $h$ - $^{11}\text{BN}$  flake with a thickness of 40 nm. The scale bar is 400 nm. (b-d) PF-SNOM images at  $1415 \text{ cm}^{-1}$  at tip-sample distances  $d$  of 1, 2 and 5 nm respectively. (e) Averaged profiles of near-field signals along the orthogonal direction to the edge, revealing an increase of polariton wavelength  $\lambda_p$  as  $d$  increases. (f) Extracted  $\omega$ - $q_p$  dispersion relation of polaritons from the  $h$ - $^{11}\text{BN}$  edge (squares, circles, and triangles) overlaid with the calculated dispersion relation (brown curve).  $q_p$  exhibits distance-dependence at all frequencies. No preferred values of polariton momentum are observed.

We hypothesize that the confinement of the circular geometry leads to the quantized

spatial frequencies in the lateral dimension. A question arises: Do polaritons behave similarly in the case of an  $h$ - $^{11}\text{BN}$  edge that lacks symmetry for the geometrical confinement? To investigate further, an edge of an  $h$ - $^{11}\text{BN}$  flake was measured by PF-SNOM (Fig. 3). The thickness of the flake is of 40 nm. The tomographic PF-SNOM images from the 3D near-field response cube at three different tip-sample distances  $d$  are shown in Fig. 3b-d. Close examination of the fringe spacing after averaging (Fig. 3e) reveals a small change of the periodicity: as tip-sample distance  $d$  increase, the periodicity also slightly increases. The extracted dispersion relation of the polaritons in the  $h$ - $^{11}\text{BN}$  flake at different tip-sample distances is displayed in Fig. 3f. In contrast to the behavior of the micro-disk, the momentum of polariton in the BN flake does not exhibit fixed values. Also, the momentum can be slightly tuned by the tip-sample distance  $d$ : longer  $d$  corresponds to a smaller momentum of the polaritons.

The comparison of the dispersion relations between the  $h$ - $^{11}\text{BN}$  micro-disk and the reflective edge confirms the above-mentioned hypothesis and suggests that the momentum of polaritons in the circular micro-disk is quantized, i.e., it has preferred values at certain frequencies. Similar to the formation of standing waves on a drum, the quantized spatial frequencies are determined by the geometry of the micro-disk and the wavelength of the hyperbolic polaritons. Modes of standing waves emerge as hyperbolic phonon polaritons propagate inside the micro-disk and are reflected by the circular edge. The standing wave solutions can be analytically described by solving a two-dimensional wave equation with boundary conditions of circular confinement. The solution is described by previous literature on  $h$ -BN nano-resonators by Equation (1) (see Supplementary Note 1 for the derivation):<sup>22</sup>

$$J'_s(k_{sn}r_0 + \phi) = 0 \quad (1)$$

where  $J_s$  is the Bessel function of  $s^{\text{th}}$  order,  $r_0$  is the disk radius,  $k_{sn}$  is the  $n^{\text{th}}$  root to Equation (1) and the spatial frequencies of the standing wave,  $n = 1, 2, 3 \dots$  and  $\phi_0$  is the anomalous phase shift at the edge, which we have found to be  $-0.28 \pi$  from fitting.

The standing wave solutions from Equation (1) have well-defined spatial frequencies. When the metallic AFM tip launches polaritons that coincide with the characteristic frequency  $k_{sn}$  of the standing wave solution, one geometrical resonant condition is formed. Consequently, the amplitude of the tip-launched polaritons is amplified at the resonant conditions at several discrete spatial frequencies.  $k_{sn}$  from the standing wave solution are marked as vertical dashed lines in Fig. 2e-f, from which we can clearly see that the fixed values of the polariton momentum are aligned with these discrete values of  $k_{sn}$ . Within the investigated frequency range, there are three resonant frequencies: 1410, 1420 and 1428  $\text{cm}^{-1}$ .

Also, when the metallic AFM tip is positioned at the nodes of the standing waves, the coupling between the EM near field of the AFM tip and the polaritonic mode is amplified, leading to an increase of the scattering signals that is measurable by PF-SNOM.

Consequently, the spatial fringes from PF-SNOM exhibit similar patterns as the amplitude square of the standing wave  $\rho^2 = J_s^2(k_{sn}r_0 + \phi)$ . Fig. 4 displays the PF-SNOM images and simulations based on the standing wave solution. Simulation details are included in Supplementary Note 1.

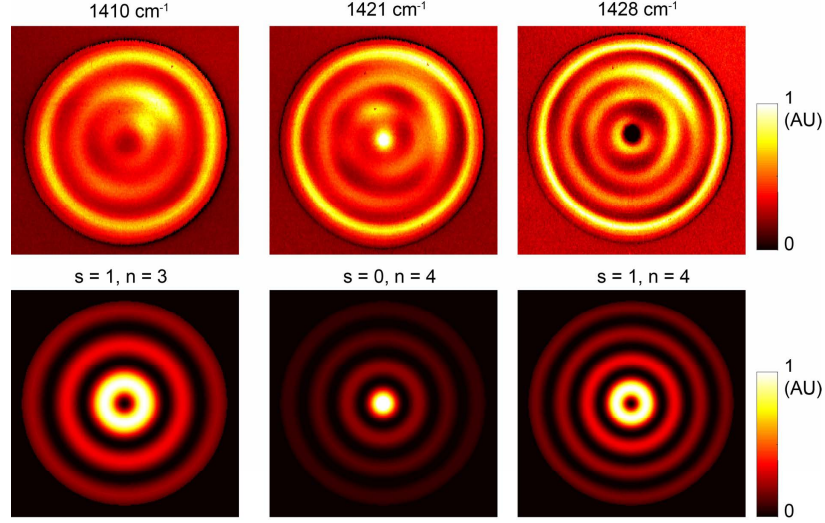


**Figure 4.** PF-SNOM images of the  $h$ - $^{11}\text{BN}$  micro-disk at  $d = 1$  nm at different resonant infrared frequencies (upper row) and their corresponding simulations of  $\rho^2$  calculated from the standing wave solutions (lower row).

In comparison, the reflective  $h$ - $^{11}\text{BN}$  edge of a large flake does not support a geometric-dependent standing wave by its own. Polaritons launched by the metallic AFM tip are not amplified at particular spatial frequencies (Fig. 3f). As a result, the dispersion relationship of the reflective edge lacks the quantization of the momentum and does not exhibit the characteristic zig-zag patterns in the dispersion relations of the  $h$ - $^{11}\text{BN}$  micro-disk in Fig. 2f.

Changing tip-sample distance can slightly tune the spatial frequency of PhP waves under conditions that lack geometrical resonance, such as in cases of the simple reflective edge and between two resonant conditions of the micro-disk (see Supplementary Fig. S4). The tuning of the spatial frequencies can be understood by the spatial distribution of the EM nearfield underneath the tip at different tip-sample distances: the tip-sample configuration with a large tip-sample distance provides a loosely enhanced EM field with low spatial frequencies; the configuration with a small tip-sample distance strongly confines the EM field that spans high spatial frequencies (Fig. 1a-b). When the tip-sample distance is small, the PhP wave with

a higher spatial frequency is excited more; when the tip-sample distance is large, the PhP wave with a lower spatial frequency is more present. On the other hand, under geometrical resonant conditions of the circular micro-disk, discrete spatial frequencies of the standing wave solutions are amplified. The small tuning of the spatial frequencies from different tip-sample distances is overshadowed by the dominant spatial frequency from the standing wave solutions. When the excitation of wavelength the PhP is between two geometric resonant conditions, the spatial frequency of the PhPs is not dominated by one standing wave, but from a superposition of two standing waves. Thus, the apparent momentum can again be tuned by the tip-sample distance. This behavior leads to the progression of the spatial fringe patterns as the tip-sample distance changes.

### **Vertical Analysis of Near-field Response**

The 3D near-field response cube contains vertical sectional information on how the signal behaves when the tip-sample distance changes. Fig. 5 displays the vertical sectional images and analysis of the  $h$ - $^{11}\text{BN}$  micro-disk. Fig. 5a shows the position where the sectional profile was taken. Fig. 5b-c displays  $S_{\text{NF}}(x, d)$  sectional image at infrared frequency of  $1420\text{ cm}^{-1}$  and  $1425\text{ cm}^{-1}$  respectively. A vertical signal range of less than 20 nm is observed, which is the dominant range of the near-field interaction between the tip and the sample. This observation can be understood by the fact that the phonon polaritons in  $h$ - $^{11}\text{BN}$  is hyperbolic PhPs that travel in the volume of the material, thus the evanescent EM field outside  $h$ - $^{11}\text{BN}$  is weak and not a part of the core component of hyperbolic PhPs inside  $h$ - $^{11}\text{BN}$ .

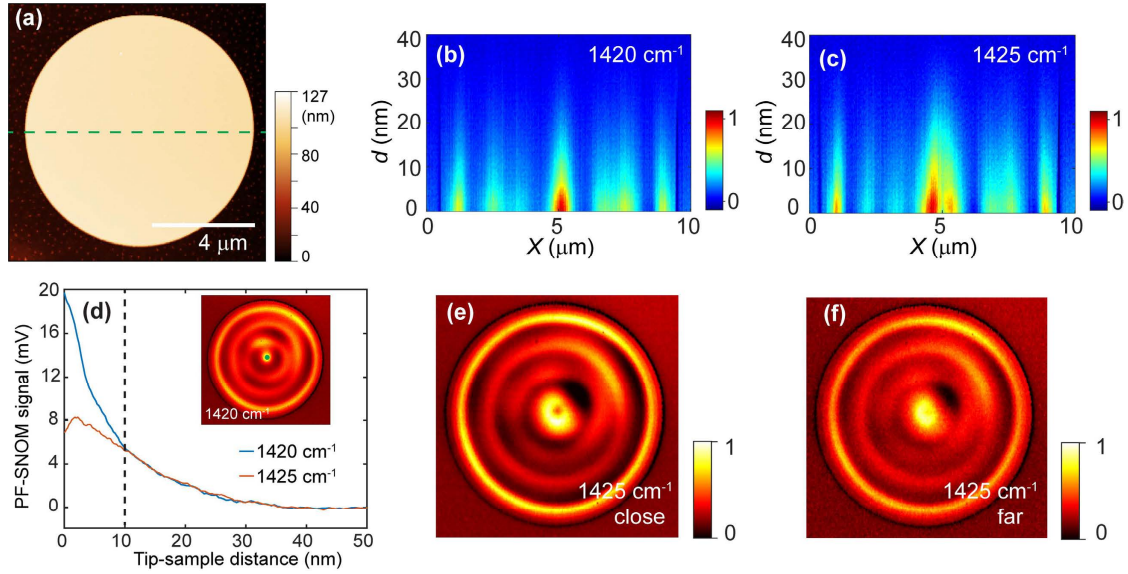


**Figure 5. Vertical sectional near-field images and analysis.** (a) AFM topography of the micro-disk. The green line across the center of the disk marks the position of vertical sectioning. (b-c)  $x$ - $d$  sectional near-field responses at  $1420\text{ cm}^{-1}$  and at  $1425\text{ cm}^{-1}$ , respectively. (d) Near-field vertical interaction curve at the center of the micro-disk at the infrared frequency of  $1420\text{ cm}^{-1}$  (blue) and  $1425\text{ cm}^{-1}$  (red). The inset shows the tomographic image of the near-field response of  $1420\text{ cm}^{-1}$  at  $d = 1\text{ nm}$ . The black dashed line is a boundary between the close ( $d < 10\text{ nm}$ ) and far range ( $d > 10\text{ nm}$ ). Within the far range, two vertical behavior curves are effectively the same. (e) Reconstructed near-field image of  $1425\text{ cm}^{-1}$  at  $d = 0\text{ nm}$ , by exponentially fitting vertical response curves of  $1425\text{ cm}^{-1}$  within the close range. The reconstructed image by fitting the data within the far range is shown in (f), in which the center dip disappears.

To examine the behavior of the vertical near-field interaction *in situ*, we read out the  $S_{\text{NF}}(d)$  responses at the center of the micro-disk at  $1420$  and  $1425\text{ cm}^{-1}$ , and display them in Figure 5d. An interesting observation appears. For the tip-sample distance region of  $d > 10\text{ nm}$ , two curves practically overlap, indicating a similar signal generation mechanism. However, at  $d < 10\text{ nm}$ , the two vertical interaction curves exhibit drastically different behavior. The curve of  $1420\text{ cm}^{-1}$  exhibits a monotonic and rapid increase as  $d$  decreases; the curve of  $1425\text{ cm}^{-1}$  exhibit a slow increase as  $d$  decreases, at a short range of  $d = 2\text{ nm}$ , the signal even starts to decrease. How do we understand this behavioral difference? The infrared frequency of  $1420\text{ cm}^{-1}$  matches the geometrical standing wave mode of the polaritons in the  $h$ - $^{11}\text{BN}$  micro disk, as revealed above;

the infrared frequency of  $1425\text{ cm}^{-1}$  is located between two resonant standing wave modes. Under the resonant condition, the near-field tip probes the same polaritonic standing wave mode regardless of the tip-sample distance. When the infrared frequency is situated between two standing wave resonant modes, the near-field tip can moderately couple to both standing wave modes and excite a superposition.

At large  $d$ , the tip-enhanced electric field weakly couples relatively more of the standing wave mode with the lower momentum; at a small  $d$ , the strongly tip-enhanced electric field excites more of the standing wave mode with the higher momentum. As the centers of two adjacent standing wave modes of the 2D Bessel Function alternate between node and antinode (Fig. 4 and Supplementary Fig. S5), the mixture of two adjacent Bessel functions leads to destructive interference between the amplitudes of the polariton wave at the center of the micro-disk. As the tip-sample distance becomes smaller, the relative strength of the standing wave mode with high momentum increases, and the destructive interference become stronger, eventually leading to the dip of the vertical interaction curve as seen in Fig. 5d. The existence of superposition is highlighted in Figs. 5e-f by reconstructing the near-field image at  $1425\text{ cm}^{-1}$  through vertical responses at small and large tip-sample distance  $d$  ranges. The difference between Figs. 5e and 5f is the proof of the destructive interference at the close  $d$  range. The non-trivial vertical decay behavior of polaritons is the manifestation of the quantization of momentum from the standing wave modes, and the shift of the mode superposition is due to the change of momentum coupling from the tip-sample distance.

## Discussions

The advantage of PF-SNOM for near-field anatomy over traditional s-SNOM analysis is

the ability to access one additional dimension along with the tip-sample distance  $d$ . In traditional s-SNOM, the spatial distribution of the  $x$ - $y$  lateral responses is collected as a nonlinearity of near-field signal over a range of tip-sample distance. The progression of the lateral spatial distribution within the cantilever oscillation range is not accessible in s-SNOM. As a result, the spectrum in the spatial frequency domain is averaged in the vertical range and inhomogeneously broadened. In contrast, the PF-SNOM directly provides lateral images with well-defined tip-sample distances  $d$  over a long distance, which enables the collection of 3D near-field response cube for near-field anatomy to identify the geometrical resonances from both tomographic and sectional images.

The momentum quantized standing wave mode of  $h$ - $^{11}\text{BN}$  micro-disk is meaningful for chemical sensing and nanophotonic applications. The geometry of the micro-disk determines the quantized momentum and corresponding resonant infrared frequencies. At the resonant frequency of the standing wave mode, the electric field is strongly enhanced and spatially localized at the center of the disk. This property suggests that the center of the  $h$ - $^{11}\text{BN}$  micro-disk may be used for chemical sensing within the upper Reststrahlen band. The geometry of the disk can be tailored to match the infrared absorption of the desirable molecules, or through the utilization of reconfigurable metal to insulator transition substrate to fine tune the PhP wavelength.<sup>23</sup> The mode quantization of isotopically pure  $h$ -BN micro-disk may serve as a momentum filter for selecting propagating PhPs of precisely defined momentum when integrated into a phonon polaritonic circuit of isotopically pure  $h$ -BN.

In conclusion, we demonstrated the near-field anatomy of an  $h$ - $^{11}\text{BN}$  microstructures with 3D near-field response cubes from PF-SNOM with both tomographic and sectional

analysis. The geometrical resonance from the standing wave solutions of the circular micro-disk leads to the quantization of the in-plane momentum of the polaritons into discrete values. Between geometrical resonant conditions from confinement and for structures that lack geometric confinement, changing the tip-sample distance fine tunes the momentum of polariton. The geometric resonance also manifests in the vertical near-field responses, leading to non-monotonic vertical behavior between standing wave modes. Three-dimensional near-field anatomy provides a new approach for *in situ* examination of polaritonic nano- and microstructures with rich information and is expected to be readily applicable to other 2D materials that support polaritons.<sup>24-27</sup>

## Methods

The PF-SNOM setup, FDTD simulation, sample preparation and calculation of the dispersion relation of  $h^{-1}$ BN are included in Supplementary Note 2.

## Acknowledgments

H.W. and X. G. X. acknowledge fruitful discussions and the help on the model simulation from Dr. Antonio Ambrosio, the help on the two-dimensional wave model and dispersion relation simulation from Dr. Michele Tamagnone and the help from Dr. William L. Wilson of Center for Nanoscale Systems of Harvard University for the fabrication of the BN micro-disk. X.G.X would like to thank Dr. Slava Rotkin and Dr. Gilbert Walker for helpful discussions. H. W. and X. G. X. thank for the support from Beckmann Young Investigator Program. J. H. E. and J. L. appreciate the support from the National Science Foundation, award number CMMI 1538127.

## References

1. Basov, D.N., Fogler, M.M. & García de Abajo, F.J. Polaritons in van der Waals materials. *Science* **354**, aag1992 (2016).
2. Agranovich, V.M. Surface Polaritons (Elsevier, 2012).
3. Dai, S. et al. Tunable Phonon Polaritons in Atomically Thin van der Waals Crystals of Boron Nitride.

- Science* **343**, 1125-1129 (2014).
4. Li, P. et al. Reversible optical switching of highly confined phonon–polaritons with an ultrathin phase-change material. *Nature Materials* **15**, 870 (2016).
  5. Caldwell, J.D. et al. Low-loss, infrared and terahertz nanophotonics using surface phonon polaritons. *Nanophotonics* (2014).
  6. Caldwell, J.D. et al. Sub-diffraction, Volume-confined Polaritons in the Natural Hyperbolic Material, Hexagonal Boron Nitride. *arXiv preprint arXiv:1404.0494* (2014).
  7. Fei, Z. et al. Infrared Nanoscopy of Dirac Plasmons at the Graphene–SiO<sub>2</sub> Interface. *Nano Letters* **11**, 4701-4705 (2011).
  8. Wang, H., Wang, L., Jakob, D.S. & Xu, X.G. Tomographic and multimodal scattering-type scanning near-field optical microscopy with peak force tapping mode. *Nature Communications* **9**, 2005 (2018).
  9. Liu, S. et al. Single Crystal Growth of Millimeter-Sized Monoisotopic Hexagonal Boron Nitride. *Chemistry of Materials* **30**, 6222-6225 (2018).
  10. Geick, R., Perry, C.H. & Rupprecht, G. Normal modes in hexagonal boron nitride. *Phys. Rev.* **146**, 543-& (1966).
  11. Dai, S. et al. Tunable phonon polaritons in atomically thin van der Waals crystals of boron nitride. *Science* **343**, 1125-9 (2014).
  12. Dai, S. et al. Subdiffractional focusing and guiding of polaritonic rays in a natural hyperbolic material. *Nat. Commun.* **6**, 6963 (2015).
  13. Yoxall, E. et al. Direct observation of ultraslow hyperbolic polariton propagation with negative phase velocity. *Nat. Photonics* **9**, 674+ (2015).
  14. Giles, A.J. et al. Ultralow-loss polaritons in isotopically pure boron nitride. *Nat. Mater.* **17**, 134-139 (2018).
  15. Folland, T.G. et al. Probing hyperbolic polaritons using infrared attenuated total reflectance microspectroscopy. *MRS Commun.* **8**, 1418-1425 (2018).
  16. Ambrosio, A. et al. Selective excitation and imaging of ultraslow phonon polaritons in thin hexagonal boron nitride crystals. *Light: Science & Applications* **7**, 27 (2018).
  17. Li, P. et al. Hyperbolic phonon-polaritons in boron nitride for near-field optical imaging and focusing. *Nature Communications* **6**, 7507 (2015).
  18. Yoxall, E. et al. Direct observation of ultraslow hyperbolic polariton propagation with negative phase velocity. *Nature Photonics* **9**, 674 (2015).
  19. Gilburd, L. et al. Hexagonal Boron Nitride Self-Launches Hyperbolic Phonon Polaritons. *The Journal of Physical Chemistry Letters* **8**, 2158-2162 (2017).
  20. Giles, A.J. et al. Ultralow-loss polaritons in isotopically pure boron nitride. *Nature Materials* **17**, 134 (2017).
  21. Dai, S. et al. Tunable phonon polaritons in atomically thin van der Waals crystals of boron nitride. *Science* **343**, 1125-1129 (2014).
  22. Tamagnone, M. et al. Ultra-confined mid-infrared resonant phonon polaritons in van der Waals nanostructures. *Sci. Adv.* **4**, eaat7189 (2018).
  23. Dai, S. et al. Phase change materials for nano-polaritonics: a case study of hBN/VO<sub>2</sub> heterostructures. *arXiv preprint arXiv:1809.09652* (2018).
  24. Hu, D. et al. Tunable Modal Birefringence in a Low-Loss Van Der Waals Waveguide. *Advanced Materials* **31**, 1807788 (2019).
  25. Zheng, Z. et al. A mid-infrared biaxial hyperbolic van der Waals crystal. *Science Advances* **5**, eaav8690

- (2019).
26. Hu, F. et al. Imaging exciton–polariton transport in MoSe<sub>2</sub> waveguides. *Nature Photonics* **11**, 356 (2017).
  27. Ma, W. et al. In-plane anisotropic and ultra-low-loss polaritons in a natural van der Waals crystal. *Nature* **562**, 557-562 (2018).

# Supplementary Materials: Three-dimensional Near-field Anatomy Reveals Geometric Resonance of Hyperbolic Phonon Polariton Micro-Structures

Haomin Wang<sup>1</sup>, Jiahan Li<sup>2</sup>, James H. Edgar<sup>2</sup>, and Xiaoji G. Xu<sup>1\*</sup>

<sup>1</sup>Department of Chemistry, Lehigh University, 6 E Packer Ave. Bethlehem, PA, 18015, USA

<sup>2</sup>Tim Taylor Department of Chemical Engineering, Kansas State University, Manhattan, Kansas 66506, USA

\*Email: [xgx214@lehigh.edu](mailto:xgx214@lehigh.edu)

**Supplementary Note 1:** Derivation of resonant conditions and calculation of fringe patterns

**Supplementary Note 2:** Methods

**Supplementary Figure S1.** s-SNOM and PF-SNOM images.

**Supplementary Figure S2.** Extraction of spatial frequencies.

**Supplementary Figure S3.** Additional PF-SNOM measurement on another  $h$ -<sup>11</sup>BN micro-disk.

**Supplementary Figure S4.** Tuning  $q_p$  by varying tip-sample distance  $d$  through PF-SNOM.

**Supplementary Figure S5.** Fringe patterns at two adjacent resonant conditions.

### Supplementary Note 1: Derivation of resonant conditions and calculation of fringe patterns

Resonant conditions of *h*-BN nano-disk resonators had been investigated thoroughly in the previous work.<sup>1</sup> According to it, the propagation of polaritons on the surface of *h*-BN micro-disk can also be described by a 2D wave equation:

$$(i\omega)^2 \rho = v_p^2(\omega) \nabla^2 \rho \quad (\text{S1})$$

in which  $\rho$  is the spatial charge density,  $v_p$  is the phase velocity and  $\omega$  is the angular frequency. Resonant conditions can be obtained by the standing wave solution of **Equation S1** using a Neumann boundary condition at the edge of disk with radius  $r_0$ , where we have:

$$\left. \frac{\partial \rho}{\partial r} \right|_{r=r_0} = 0 \quad (\text{S2})$$

Solutions of the 2D wave equation are in forms of Bessel function with polar coordinate  $(r, \theta)$ :

$$\rho = J_s(kr)(A \cos(s\theta) + B \sin(s\theta))e^{i\omega t} \quad (\text{S3})$$

in which  $J_s$  is the Bessel function of  $s^{\text{th}}$  order,  $k$  is the wave vector of polariton and  $A, B$  are arbitrary complex amplitudes. By solving **Equation S1** and **S2** together, one can get standing wave solutions that represents the resonant conditions of a circular disk:

$$\begin{aligned} \rho &= J_s(k_{sn}r + \phi)(A \cos(s\theta) + B \sin(s\theta))e^{i\omega t} \\ &\text{with } k_{sn} = n^{\text{th}} \text{ root of } J'_s(kr_0 + \phi) = 0 \end{aligned} \quad (\text{S4})$$

Note that a correction phase factor  $\phi$  is added to account for the extra phase shift of polariton waves that have been reflected by the disk edge. In our case, we found  $\phi = -0.28\pi$  best fit our experimental results, which agrees well with  $-0.28\pi$ <sup>1</sup> and  $-0.25\pi$ <sup>2,3</sup> found in literatures.

Measuring  $\rho$  at different non-resonant and resonant conditions with an AFM tip and illumination light results to different signal contributions. The majority of PF-SNOM signal is from the so-called roundtrip component, which is circularly symmetric and independent of  $\theta$ .<sup>1</sup> Thus, we can estimate PF-SNOM signal as roundtrip component:

$$\text{PF-SNOM signal} \propto \rho^2 = J_s^2(k_{sn}r + \phi) \quad (\text{S5})$$

which can be used to calculate fringe patterns that we've seen in PF-SNOM images. Since the anomalous phase shift  $\phi$  affects most the outermost fringe and cannot be easily accounted due to the presence of fringing field,<sup>1</sup> in our simulation of  $\rho^2$  we omit this term to achieve optimal agreement between simulated fringes and PF-SNOM fringes.

Solving **Equation S4** gives out a series of  $k_{sn}$ , which should be relevant to experimentally observed resonant conditions. To assign a proper  $(s, n)$  pair to each resonant condition, we compare  $k_{sn}$  with  $q_p$  from FFT on PF-SNOM images at resonant conditions. The workflow is shown below:

1. Obtain resonant  $q_p$  from experimentally observed PF-SNOM images. In our case, we chose

PF-SNOM images at 1410, 1421, and 1428  $\text{cm}^{-1}$  as three resonant conditions (since the momentum is locked no matter the change of tip-sample distance). Experimental fringe patterns at each resonant condition were extracted by performing a radial averaging from the disk center on each of resonant PF-SNOM image. Then, FFT was performed on each fringe pattern to get spatial frequency of the fringe  $k_f$ , which then was converted to the momentum of polariton  $q_p$  by  $q_p = \pi k_f$ .

2. A series of  $k_{sn}$  from solutions of **Equation S4** were plugged back into **Equation S5** to get simulated fringe patterns  $\rho^2$ .
3. Compare  $k_{sn}$  with  $q_p$  and  $\rho^2$  with experimental fringe patterns. If they both match, assign corresponding mode numbers  $(s, n)$  to this resonant frequency.

Parameters that are used in these steps for resonant conditions shown in the main text **Figs. 2e-f** are summarized in **Table S1**, from which we found that the resonances that we observed by PF-SNOM mainly correspond to modes with  $s = 0$  or 1.  $s = 0$  corresponds to modes that show the maximal signal at disk center, while  $s = 1$  corresponds to modes that show the minimal at disk center (**Supplementary Fig. S5**).

**Table S1** Parameters used in the assignment of  $(s, n)$

Resonant frequencies ( $\text{cm}^{-1}$ )	$q_p$ ( $\mu\text{m}^{-1}$ )	$(s, n)$	$k_{sn}$ ( $\mu\text{m}^{-1}$ )	Parameters used in solving <b>Eq. S4</b>
1410	2.11	(1,3)	2.08	$\phi = -0.28\pi$ $r_0 = 4.5 \mu\text{m}$
1421	2.48	(0,4)	2.44	
1428	2.84	(1,4)	2.78	

## Supplementary Note 2: Methods

### Materials

The sample were prepared starting from a silicon wafer with 285 nm of thermal oxide. Optical lithography and gold evaporation were used to define alignment markers. Subsequently, the wafer was diced into chips. Isotopically pure  $h$ - $^{11}\text{BN}$  crystal flakes were grown from a molten metal nickel-chromium solution using monoisotopic boron-11 as the boron source.<sup>4</sup> The  $h$ - $^{11}\text{BN}$  was exfoliated using the Scotch tape technique and transferred on the substrate. The excess of glue was removed with acetone and IPA. E-beam lithography with ZEP resist was performed on the flakes and was followed by reactive ion etching with a fluorine-based

recipe. Subsequently, ZEP was removed with remover PG, and the sample was rinsed with acetone and IPA.

### PF-SNOM setup

The PF-SNOM setup used in this work is composed of an AFM (Bruker Multimode 8 with Nanoscope V controller with peak force tapping), a frequency tunable quantum cascade laser (QCL) (MIRcat, Daylight Photonics), a mercury cadmium telluride (MCT) infrared detector (KLD series, Kolmartech), and data acquisition devices (PXI-5122 and PXI-4461, National Instruments). Gold-coated AFM tips (HQ:NSC15/CR-AU, Mikromasch) were used. The infrared beam from QCL was focused on the tip apex with a gold-coated parabolic mirror (numerical aperture of 0.25) during experiments. The scattered light from the tip-sample region was collected by the same parabolic mirror, and then directed to the MCT detector. The light path of infrared laser was adjusted to maximize detected near-field signals. During the experiment, the AFM was operated in the peak force tapping mode of 4 kHz, where the tip is hold stationary and the peak-to-peak oscillation amplitude of the sample stage is set as 300 nm. Scattered signals from the MCT detector, cantilever deflection signals from the quadrant photodiode of AFM, and applied piezo voltages ( $x$  and  $y$ ) from AFM are all recorded by two data acquisition devices simultaneously. In Figs. 1c-d, cantilever deflection and scattered signals from average of 200 cycles of peak force tapping were used. In all other PF-SNOM measurement, signals are from the average of 60 cycles. A custom script is used (MATLAB R2018b) to convert the raw data into a 3D response cube to get PF-SNOM images at different tip-sample distances, vertical near-field interaction curves, etc. The conversion between the time domain and the tip-sample distance domain and the algorithm to subtract far-field backgrounds are the same as described in the literature.<sup>5</sup>

### FDTD simulation

FDTD simulations in Figs. 1a-b were achieved by the Lumerical FDTD software (Lumerical Inc.). A gold cone with the end radius of 30 nm was used to simulate the AFM tip, and a Si disk with a radius of 4  $\mu\text{m}$  and thickness of 80 nm was placed under the tip by a separation of 1 or 10 nm. The IR dielectric constant  $\varepsilon = 11.7$  for Si<sup>6</sup> was used. The light source was set to be a p-polarized plane wave with an amplitude of 1 arbitrary unit and an incident angle of 15° to mimic the actual incident angle from the parabolic mirror.

### Dispersion relation simulation

The calculated dielectric function of  $h^{-1}\text{BN}$  in Fig. 2a is based on Equation (S6):<sup>7,8</sup>

$$\begin{cases} \varepsilon_{\perp} = \varepsilon_{\infty,\perp} + \varepsilon_{\infty,\perp} \frac{\omega_{\text{LO},\perp}^2 - \omega_{\text{TO},\perp}^2}{\omega_{\text{TO},\perp}^2 - \omega^2 - i\omega\Gamma_{\perp}} \\ \varepsilon_{\parallel} = \varepsilon_{\infty,\parallel} + \varepsilon_{\infty,\parallel} \frac{\omega_{\text{LO},\parallel}^2 - \omega_{\text{TO},\parallel}^2}{\omega_{\text{TO},\parallel}^2 - \omega^2 - i\omega\Gamma_{\parallel}} \end{cases} \quad (\text{S6})$$

where  $\varepsilon_{\perp}$  and  $\varepsilon_{\parallel}$  are in-plane ( $x$  and  $y$ ) and out-of-plane ( $z$ ) dielectric functions;  $\varepsilon_{\infty}$  is high-frequency permittivity;  $\omega$  is the frequency of incident light;  $\omega_{\text{LO}}$  and  $\omega_{\text{TO}}$  are longitudinal and transverse optical

phonon mode frequencies, and  $\Gamma$  is the phonon damping. Parameters of  $h$ - $^{11}\text{BN}$  are from Giles *et al.*<sup>9</sup>, and are summarized in Table S2:

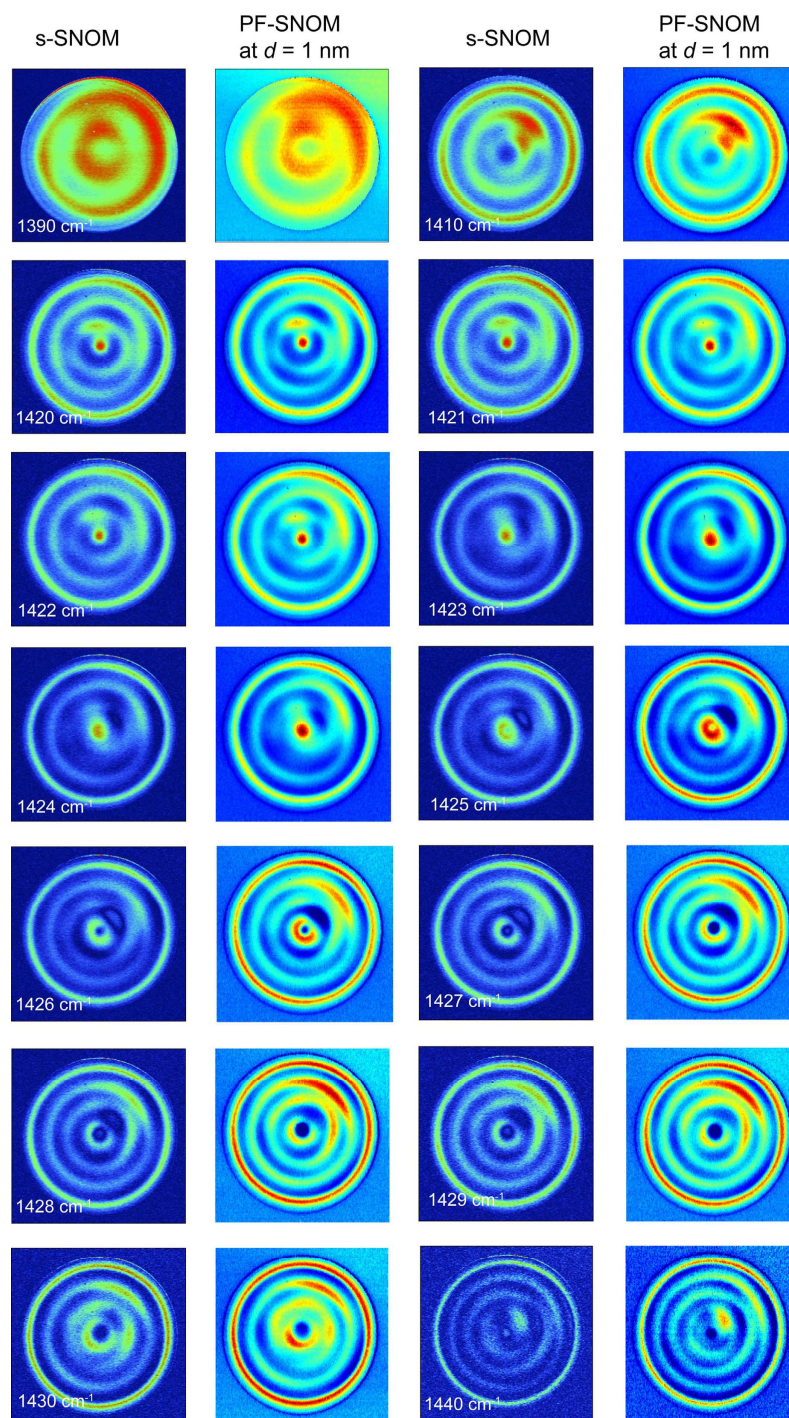
**Table S2. Fitting parameters of  $h$ - $^{11}\text{BN}$**

$\varepsilon_{\infty,\perp}$	$\omega_{\text{LO},\perp}$ ( $\text{cm}^{-1}$ )	$\omega_{\text{TO},\perp}$ ( $\text{cm}^{-1}$ )	$\Gamma_{\perp}$ ( $\text{cm}^{-1}$ )	$\varepsilon_{\infty,\parallel}$	$\omega_{\text{LO},\parallel}$ ( $\text{cm}^{-1}$ )	$\omega_{\text{TO},\parallel}$ ( $\text{cm}^{-1}$ )	$\Gamma_{\parallel}$ ( $\text{cm}^{-1}$ )
5.32	1608.7	1359.8	2.1	3.15	814	755	1

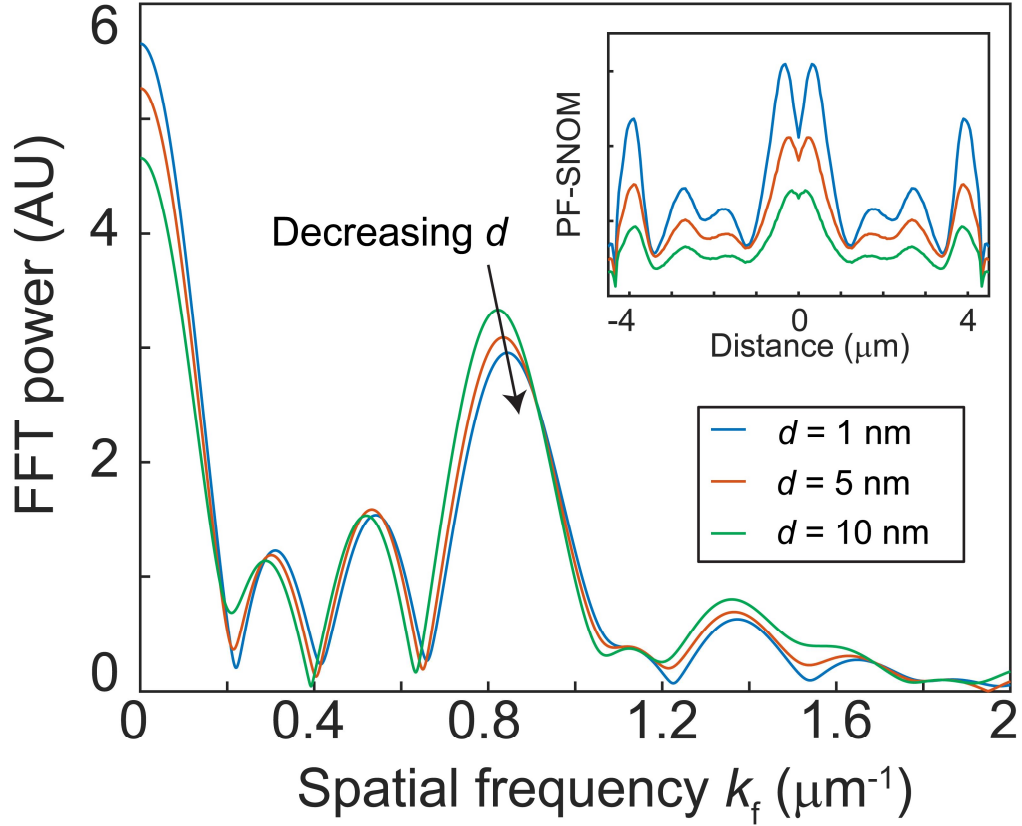
The  $\omega - q_{\text{p}}$  dispersion relation (brown curves in Figs. 2e-f) is calculated based on the air/ $h$ -BN/SiO<sub>2</sub> structure according to Equation (S7):<sup>7,8</sup>

$$q_{\text{p}} = \frac{i\sqrt{\varepsilon_{\parallel}}}{z\sqrt{\varepsilon_{\perp}}} [\arctan(-i\varepsilon_{\text{a}}\sqrt{\varepsilon_{\parallel}\varepsilon_{\perp}}) + \arctan(-i\varepsilon_{\text{s}}\sqrt{\varepsilon_{\parallel}\varepsilon_{\perp}}) + \pi l] \quad (\text{S7})$$

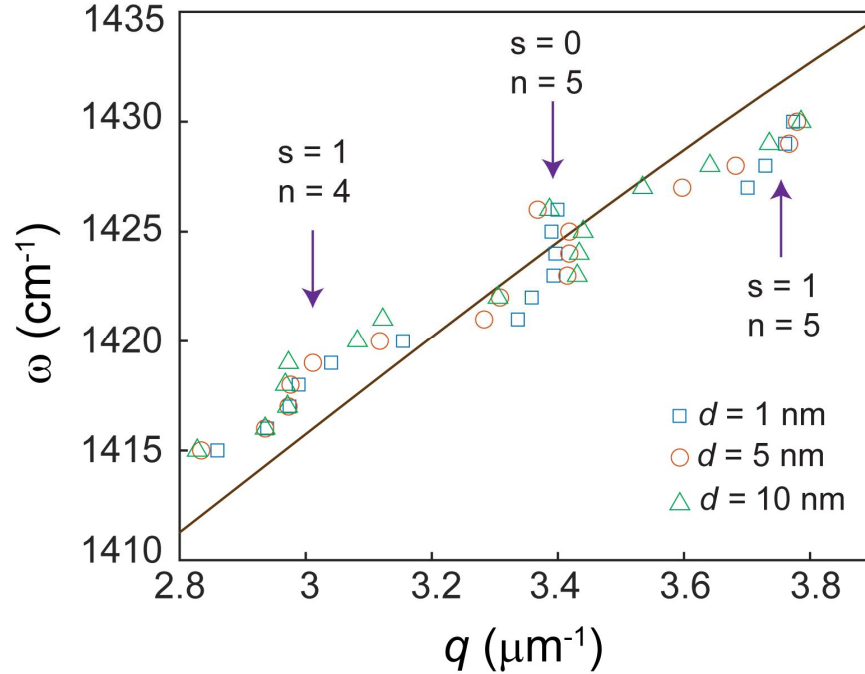
where  $z$ ,  $\varepsilon_{\text{a}}$ ,  $\varepsilon_{\text{s}}$  are the thickness of  $h$ - $^{11}\text{BN}$ , dielectric functions of air and SiO<sub>2</sub> substrate, respectively. We use  $z = 70$  nm,  $\varepsilon_{\text{a}} = 1$ , and  $\varepsilon_{\text{s}} = 2.05$ . The permittivity of SiO<sub>2</sub> is modified as 2.05 instead of 1, because the SiO<sub>2</sub> layer is not perfectly homogeneous in our case.



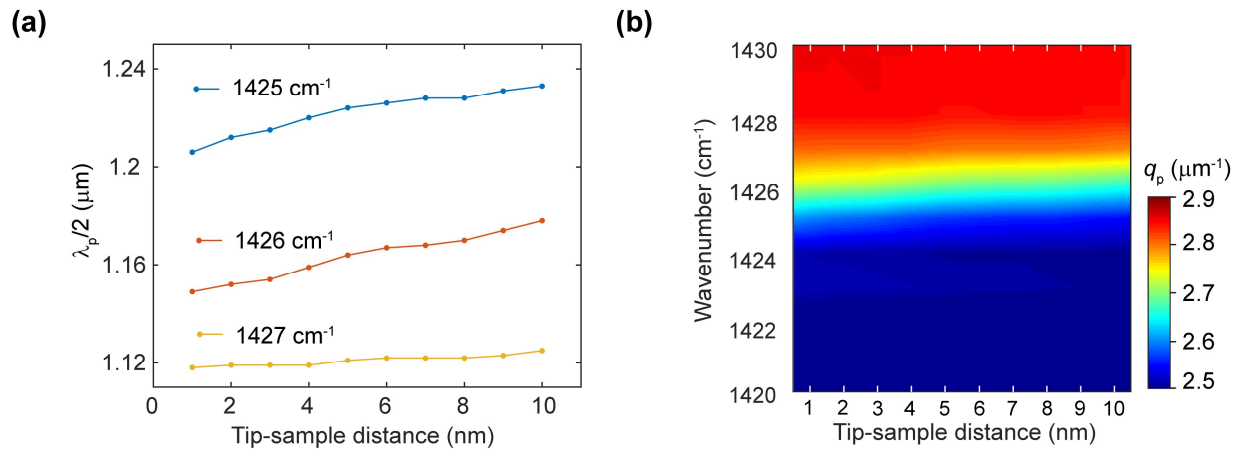
**Supplementary Figure S1.** s-SNOM and PF-SNOM images. s-SNOM images are obtained using the same homodyne setup as PF-SNOM. The AFM tip is mechanically driven by a piezo at its mechanical resonant frequency of 220 kHz. Scattered signals from the detector are routed into a lock-in amplifier, which demodulates the signal with the reference frequency of 220 kHz, the lock-in amplitude of 4<sup>th</sup> harmonic (880 kHz) is used to produce the near-field image.



**Supplementary Figure S2.** Extraction of spatial frequencies. Fringe patterns at  $\omega = 1425 \text{ cm}^{-1}$  and  $d = 1, 5, 10 \text{ nm}$  are extracted through radial averaging from the center of micro-disk and are displayed in the inset. The same procedure is applied to PF-SNOM images at other  $\omega$  and  $d$ . Resulting fringe patterns are then Fourier Transformed to obtain the spatial frequency of the fringe  $k_f$ , and to get the polariton momentum  $q_p$  by  $q_p = \pi k_f$ .

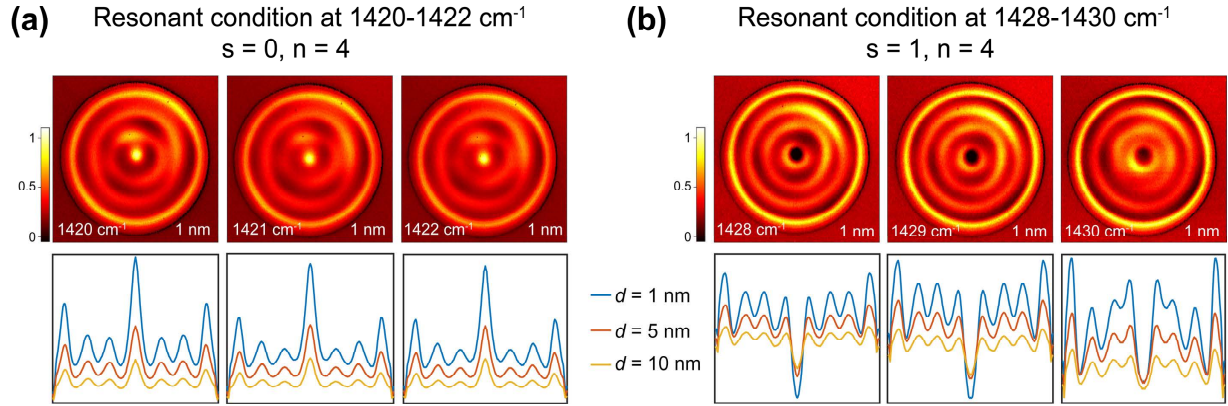


**Supplementary Figure S3.** Additional PF-SNOM measurement on another  $h^{-1}\text{BN}$  micro-disk. The thickness is 60 nm, and the diameter is 8.9  $\mu\text{m}$ . Experimental data (blue squares, orange circles and green triangles) are overlaid with calculated dispersion relation (brown curve) and resonant conditions (vertical purple arrows, with assigned  $(s, n)$  numbers). Similar to Figs. 2e-f in the main text, polariton momentum  $q_p$  is less dependent of tip-sample distance  $d$  at resonant conditions, and changes at different  $d$  at non-resonant conditions.



**Supplementary Figure S4.** Tuning  $q_p$  by varying tip-sample distance  $d$  through PF-SNOM. (a) Under non-resonant conditions such as  $\omega = 1425, 1426$  and  $1427 \text{ cm}^{-1}$ , the wavelength of the fringe pattern  $\lambda_f$ ,

polariton wavelength  $\lambda_p = 2\lambda_f$  and polariton momentum  $q_p = \frac{2\pi}{\lambda_p}$  can be tuned by changing tip-sample distance  $d$ . As this figure shows, as  $d$  increases from 1 to 10 nm,  $\lambda_f$  increases from 1.206, 1.149, 1.118 to 1.233, 1.178 and 1.125  $\mu\text{m}$  for 1425, 1426 and 1427  $\text{cm}^{-1}$ , respectively. (b) A false colormap of polariton momentum  $q_p$  over  $\omega = 1420\text{--}1430 \text{ cm}^{-1}$  and  $d = 1\text{--}10 \text{ nm}$ . At resonant conditions ( $\omega = 1420\text{--}1422$  and  $1428\text{--}1430 \text{ cm}^{-1}$ ),  $q_p$  does not change with  $d$ . On the contrary, at non-resonant conditions ( $\omega = 1423\text{--}1426 \text{ cm}^{-1}$ ),  $q_p$  increases as  $d$  increases. These results demonstrate that PF-SNOM is capable of tuning  $q_p$  under non-resonant conditions and indicate that PF-SNOM can also be used to distinguish whether the system has extrinsic resonance.



**Supplementary Figure S5.** Fringe patterns at two adjacent resonant conditions. According to PF-SNOM experimental results and model prediction (**Figs. 3b-c** in the main text), resonant momentum  $q_p(s, n)$  increases with the increase of incident frequency  $\omega$  with alternating  $s$  between 0 and 1. In addition, the roundtrip component that we observed in PF-SNOM can be approximated as a square of the Bessel function (**Equation S5**). If we plug  $r = 0$  (disk center) into **Equation S5** and omit the anomalous phase shift  $\phi$ , we will get  $\rho^2 = J_s^2(0)$ , which are constants determined simply by the order  $s$  of Bessel function. With  $s = 0$  and 1 alternating, we see PF-SNOM signal at the disk center alternating from bright ( $s = 0, J_0^2(0)$  is local maximum) to dark ( $s = 1, J_1^2(0)$  is local minimum).

## References

1. Tamagnone, M., Ambrosio, A., Chaudhary, K., Jauregui, L.A., Kim, P., Wilson, W.L. & Capasso, F. Ultra-confined mid-infrared resonant phonon polaritons in van der Waals nanostructures. *Science Advances* **4**, eaat7189 (2018).
2. Giles, A.J., Dai, S., Glembocki, O.J., Kretinin, A.V., Sun, Z., Ellis, C.T., Tischler, J.G., Taniguchi, T., Watanabe, K. & Fogler, M.M. Imaging of anomalous internal reflections of hyperbolic phonon-polaritons in hexagonal boron nitride. *Nano letters* **16**, 3858-3865 (2016).

3. Nikitin, A.Y., Low, T. & Martin-Moreno, L. Anomalous reflection phase of graphene plasmons and its influence on resonators. *Physical Review B* **90**, 041407 (2014).
4. Folland, T.G., Maß, T.W., Matson, J.R., Nolen, J.R., Liu, S., Watanabe, K., Taniguchi, T., Edgar, J.H., Taubner, T. & Caldwell, J.D. Probing hyperbolic polaritons using infrared attenuated total reflectance micro-spectroscopy. *MRS Communications* **8**, 1418-1425 (2018).
5. Wang, H., Wang, L., Jakob, D.S. & Xu, X.G. Tomographic and multimodal scattering-type scanning near-field optical microscopy with peak force tapping mode. *Nature Communications* **9**, 2005 (2018).
6. Dunlap, W.C. & Watters, R.L. Direct Measurement of the Dielectric Constants of Silicon and Germanium. *Physical Review* **92**, 1396-1397 (1953).
7. Dai, S., Fei, Z., Ma, Q., Rodin, A.S., Wagner, M., McLeod, A.S., Liu, M.K., Gannett, W., Regan, W., Watanabe, K., Taniguchi, T., Thiemens, M., Dominguez, G., Neto, A.H.C., Zettl, A., Keilmann, F., Jarillo-Herrero, P., Fogler, M.M. & Basov, D.N. Tunable Phonon Polaritons in Atomically Thin van der Waals Crystals of Boron Nitride. *Science* **343**, 1125-1129 (2014).
8. Zhao, B. & Zhang, Z.M. Perfect mid-infrared absorption by hybrid phonon-plasmon polaritons in hBN/metal-grating anisotropic structures. *International Journal of Heat and Mass Transfer* **106**, 1025-1034 (2017).
9. Giles, A.J., Dai, S., Vurgaftman, I., Hoffman, T., Liu, S., Lindsay, L., Ellis, C.T., Assefa, N., Chatzakis, I., Reinecke, T.L., Tischler, J.G., Fogler, M.M., Edgar, J.H., Basov, D.N. & Caldwell, J.D. Ultralow-loss polaritons in isotopically pure boron nitride. *Nature Materials* **17**, 134 (2017).